Degradation paths of manganese-based MOF materials in a model oxidative environment: a computational study

Elena V. Khramenkova,[a] Mikhail V. Polynski,[a,*] Alexander V. Vinogradov,[a] Evgeny A. Pidko[a,b,*]

Stability is the key property of functional materials. In this work we investigate computationally the degradative potential of a model Mn-BTC (BTC = benzene-1,3,5-tricarboxylate) metal-organic framework (MOF) building block in aqueous solutions under oxidative conditions. Model density functional theory calculations have shown that the direct hydrolysis of the Mn-containing moieties is more difficult than their decomposition via the oxidation-induced paths. While the interaction with H_2O_2 species is of non-covalent nature and requires O-O-bond breaking to initiate Mn-center oxidation, open-shell O_2 species readily oxidize radical Mn-centers and form bonds of σ-, π-, or δ-symmetry with the metal. The oxidative transformations of di-Mn paddle-wheel carboxylate structure forming units are accompanied with substantial distortions of the coordination polyhedra that, together with the increased Lewis acidity of the oxidized metal centers, facilitates the hydrolysis leading to the degradation of the structure at a larger scale. Whereas such a mechanism is expected to hamper the catalytic applications of such Mn-MOFs, the associated structural response to oxidizing and radical species can create a basis for the construction of Mn-MOF-based drug delivery systems with increased bio-compatibility.

1. Introduction

Metal-organic frameworks (MOFs) are crystalline nanoporous structures, which consist of metallic coordination centers and organic ligands.[1,2] The key features of these materials are high crystallinity and well-defined highly porous structure along with unprecedented structural and functional tunability.[3,4] MOF-based materials and devices show a great promise for various applications ranging from gas sorption[5] and separation of enantiomers[6] to photonics[7] and catalysis.[8,9] Long-term stability and ability to preserve a well-defined structure of the framework under operating conditions are the necessary features in the large-scale implementation of MOF-based systems and the lack of these may hamper their wide application.[10–12]

Fundamentally different requirements to material properties arise in case of their biomedical applications. There is a growing interest to the utilization of inorganic chemistry polymers including MOFs in the development of multifunctional biomedical materials.[13,14] Here, the intrinsic instability of the hybrid organic-inorganic framework can be regarded as an advantageous feature enabling programmed degradation of the material.[15,16] The possibility of the programmed decomposition of an inorganic matrix into molecular building blocks[17,18] facilitates its removal from the organism as well as drives the controlled and targeted release of bio-active materials.[19,20] Therefore, MOFs are considered promising for the construction of responsive matrices and carriers for smart drug delivery systems.[21,22] Their predictable and tunable on the molecular level chemistry creates a possibility to design chemical response mechanisms to varying environmental conditions, i.e.[23] one can design these materials to respond to specific changes in the microenvironment of pathological tissues. Acidosis, elevated tissue temperature, and formation of reactive oxygen species (ROS) are the specific signals that can direct the targeted delivery of an active pharmaceutical ingredient (API) to a pathologic area.[24–26] MOFs readily satisfy the essential requirements for smart drug delivery platforms, which are controllable degradation, biocompatibility and simplicity of chemical functionalization. They may be synthesized from biocompatible components as non-toxic metals and organic ligands. The medical use of widely explored Fe- and Cr-based MOFs is limited due to the toxicity issues although such MOFs are able to upload high amounts of API.[27] In this context, Mn-based inorganic systems are particularly appealing due to their low toxicity combined with Mn rich coordination chemistry. While being toxic only in high dosage,[28] Mn regulates biological processes and is a component of many enzymes.[29–31]

Mn-based MOFs are also considered as catalysts for a number of important chemical processes. In particular, such Mn-MOFs as $[Mn_3(atpa)_3(dmf)_2]$ and $[Mn_2(tpa)_2(dmf)_2]$ were investigated as effective Lewis acid catalysts for the cyanosilylation of acetaldehyde (atpa = 2-aminoterephthalate, tpa = terephthalate, dmf = dimethylformamide).[32] The oxidative degradation of phenol catalyzed by bimetallic Fe/Mn-MOF-71 was studied by Sun et al.[33] According to Pereira et al[34] Mn-based PIZA, RPM and ZJU MOF families are catalytically active for alkane oxidation.

[a] *TheoMAT group, International Laboratory "Solution Chemistry of Advanced Materials and Technologies", ITMO University, Lomonosova str. 9, St. Petersburg 191002, Russia, E-mail: polynskimikhail@gmail.com*

[b] *Inorganic Systems Engineering group, Department of Chemical Engineering, Faculty of Applied Sciences, Delft University of Technology, Van der Maasweg 9, 2629 HZ Delft, The Netherlands, E-mail: E.A.Pidko@tudelft.nl*

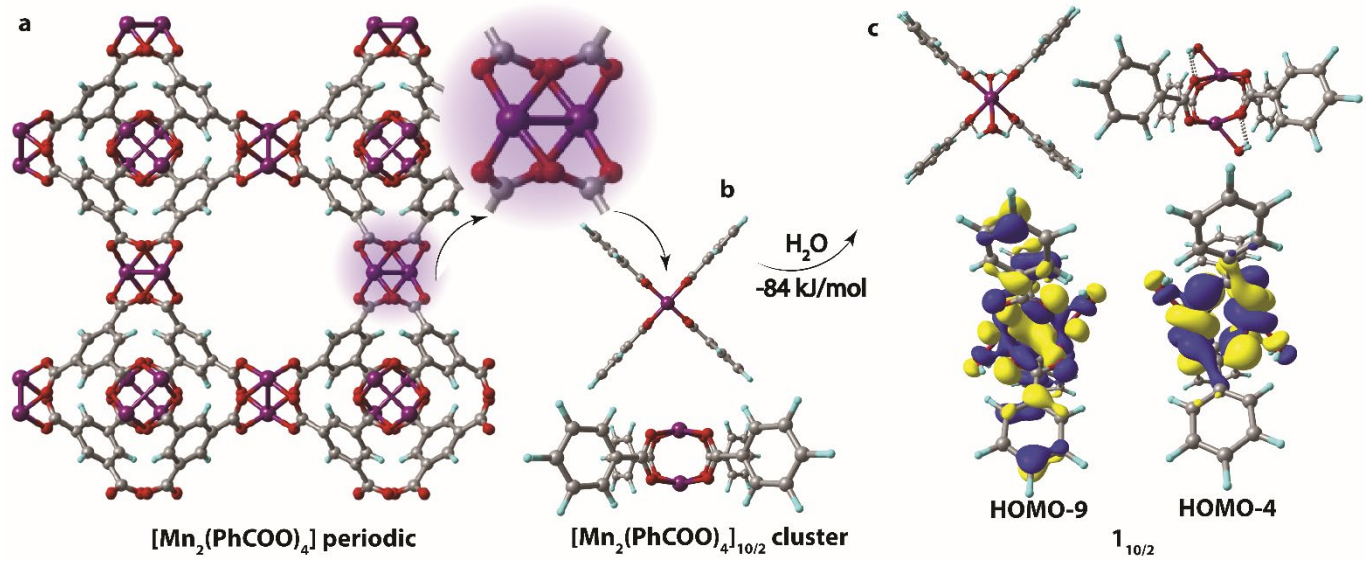

Figure 1. The periodic structure of (a) Mn-BTC MOF and (b) the corresponding $[Mn_2(PhCOO)_4]$ cluster model in s = 10/2 spin state; (c) the $\mathbf{1}_{10/2}$ aqua-complex along with the MOs representing the relevant molecular orbitals responsible for the Mn-H_2O binding (isosurface thresholds are 0.012 and 0.018 for HOMO-4 and HOMO-9 respectively). (b) and (c) optimized at the PBE-D3/6-31G(d,p) level of theory. Oxygen atoms are red, manganese atoms are purple, carbon atoms are grey, and hydrogen atoms are blue.

The behavior of Mn-based MOFs in oxidative environment has been a subject of several experimental studies. Depending on the nature of the ligands and MOF structure, the intrinsic structural stability under harsh reaction conditions may vary substantially.[35–37] Zuluaga et al. have reported Mn-MOF-74 (Mn_2(DOBDC), DOBDC = 2,5-dioxido-1,4-benzenedicarboxylic acid) susceptibility to hydrolysis that led to the degradation of the structure and limited the sorption capacity of the material.[38] On the other hand, the report by Wu et al. demonstrated a perfect structural stability of a defected Mn-MOF-74 when exposed to water for up to 7 days.[39] The same framework material has been further employed for the catalytic oxidation of alkylaromatics in an O_2 flow.[40] Hansen et al. reported a Mn-based catalyst featuring 2,2':6',2''-terpyridine structure-forming ligands as an active oxidation catalyst capable of retaining structural integrity in the catalytic oxidative environment.[41] MOF structures featuring Mn(+3)-porphyrin catalytic motifs have been reported as active and highly durable olefin oxidation catalysts.[42] An alternative IRMOF-3(Mn) catalyst made of Mn-carboxylate units was also found to be stable under the conditions of the gas-phase selective oxidation of alkanes.[43] Importantly, a wide range of catalytic studies explored the reactivity of Mn-MOFs in non-aqueous media.[42–46] In biological systems, the aqueous environment may potentially open a possibility for either direct or oxidation-induced hydrolysis as the routes for controlled decomposition of Mn-MOF. The stability of materials in oxidative environment has been the subject of computational studies as well.[47–49]

The interaction of MOF-based materials with the oxidizing species is thus of key importance for pharmaceutical chemistry and catalysis. The knowledge of the corresponding mechanisms on the molecular level may help to determine whether, on the one hand, a MOF material under consideration will irreversibly interact and (controllably) degrade under oxidative conditions. The understanding of controllable degradation mechanisms will allow for the construction of new targeted drug delivery systems. On the other hand, the material may be stable towards oxidizing species reacting reversibly and activating them. Therefore, the understanding of the MOF-oxidizing specie interaction mechanism may direct new oxidation catalyst development as well.

The focus of the presented computational study is the reactivity of Mn-BTC framework (BTC = benzene-1,3,5-tricarboxylate, Fig. 1a) towards oxidizing species (O_2 and H_2O_2) in aqueous media. We show that the oxidative transformations of the Mn centers in MOFs can potentially be employed as the driver to controlled degradation of Mn-MOF-based nanocontainers in response to increased levels of oxidants produced in pathologic tissues. We have computationally evaluated the energetics of the reaction mechanisms corresponding to the MOF-O_2- and MOF-H_2O_2-interactions in aqueous media. The results provide the guidance towards the further design of responsive structures for a wider range of application including smart drug systems. Besides, the insights into the processes determining the structural (in)stability of Mn-BTC frameworks under oxidative conditions are crucial for their utilization in oxidation catalysis.

2. Computational methods

Density functional theory (DFT) calculations were performed using the Gaussian 09 D.01[50] program suite to study the structural properties of Mn-BTC MOF and elucidate its stability towards the oxidizing species (O_2 and H_2O_2) in water. Similar to our previous work on a MOF-based drug delivery system,[51] all calculations were carried out at the PBE-D3/6-311++G(d,p)//PBE-D3/6-31G(d,p) level of theory.[52,53] Dispersion attraction was accounted for with empirical

correction scheme proposed by Grimme.[54] Bulk solvent effects (water) were accounted with PCM solvation model[55] applied to single point calculations at the PBE-D3/6-311++G(d,p) level while the short range interaction of Mn centers in Mn-BTC with H_2O molecules was accounted for by the explicit inclusion of H_2O species in the model systems. Vibrational frequencies were calculated analytically to evaluate the nature of the optimization-obtained stationary points.

The interaction with O_2 and H_2O_2 molecules and local structural deformations that could initiate the material degradation processes were investigated in the cluster-continuum approach. The cluster model representing the Mn-carboxylate paddle-wheel configuration was cut from a periodic structure of Mn-BTC MOF (Fig. 1a). The resulting cluster fragment of $[Mn_2(PhCOO)_4]$ was then coordinatively saturated by the inclusion of two water molecules. The geometries of all cluster models were optimized without any geometry constraints to satisfactory represent the substantial geometrical flexibility and relaxation potential of the coordination polymers.[56,57] The effect of possible steric inflexibility was tested by the set of constrained optimizations, in which the positions of the para-H atoms of the $PhCOO^-$ units were fixed. These constrained test optimizations were carried out on the configurations corresponding to the most stable (in terms of exothermicity of formation) and distorted complexes obtained through the unconstrained optimizations. The computed energetics and optimized structures are summarized in the Supporting Information for the article (Fig. S1, Fig. S2 and Table S1). These tests evidence key role of the structural flexibility for the preservation of the optimal coordination environment of the Mn centers. The excessive geometrical strain imposed by the fixed positions of the para-H-atoms in $PhCOO^-$ ligands gave rise to the decoordinaton of Mn-centers in some cases.

All $L[Mn_2(PhCOO)_4]L$ model complexes (where L is H_2O, H_2O_2, or O_2) were considered in various spin states (namely, S = 6/2, 8/2, 10/2) while in the case of $H_2O[Mn_2(PhCOO)_4]O_2$ and $O_2[Mn_2(PhCOO)_4]O_2$ complexes, S = 12/2 and 14/2 spin states were also considered. Initial test calculations indicated that the other electronic configurations (including the lower-spin and broken symmetry configurations, see below) are characterized by excessively high energies and therefore are not relevant to the processes considered here.

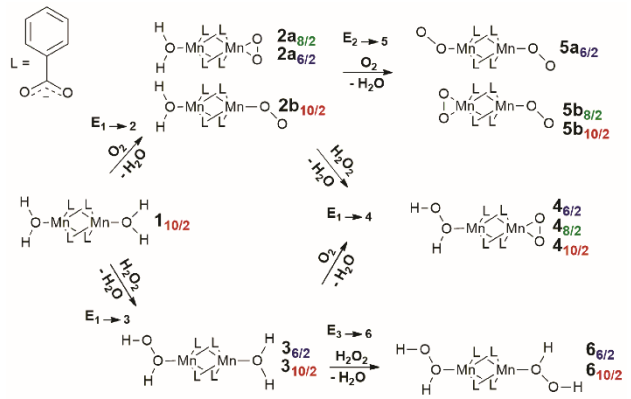

Scheme 1. A stepwise path for coordination of oxidizing species to $\mathbf{1_{10/2}}$ complex.

The concurrent adsorption energies (E_{ads}) of the oxidizing species were calculated according to the formula:

$E_{ads} = En\text{-}_{OX\text{-}Mn\text{-}BTC} + nE_{H2O} - E_{AQUA} - nE_{OX}$

where $En\text{-}_{OX\text{-}Mn\text{-}BTC}$ is the total energy of the $L[Mn_2(PhCOO)_4]L$ complex, E_{AQUA} is the energy of aqua-complex further designated as $\mathbf{1_{10/2}}$ (Fig. 1c), E_{H2O} and E_{OX} are, respectively, the total energies of H_2O and O_2 or H_2O_2 molecules, and n is the number of H_2O molecules substituted in the process.

The molecular orbital isosurfaces used for the analysis of bonding in the adsorption complexes were constructed with the ChemCraft program.[58]

3. Results and discussion

3.1. Starting configurations

The structure unit of Mn-BTC metal-organic framework (Fig. 1a) was modeled as $[Mn_2(PhCOO)_4]$ cluster (Fig. 1b). The structure of Mn-BTC is represented by a periodic array of dimeric Mn^{2+} paddle-wheel centers linked by four benzene-1,3,5-tricarboxylic ligands (BTC). A number of spin states is accessible to the dimeric $[Mn_2(PhCOO)_4]$ species since the carboxylate ligand are formally considered of weak-field class. Particularly, 6/2, 8/2, 10/2 spin configurations as well as the broken symmetry singlet state were considered. In the case of $[Mn_2(PhCOO)_4]$ cluster, high-spin s=10/2 state with the square-planar coordination of the Mn^{2+} cations having the paddle-wheel structure was the most energetically favorable. The lower spin-states of S = 6/2 and 8/2 were less favorable (by 10 and 19 kJ/mol), respectively. To ensure the unlikeliness of the singlet state with the antiferromagnetic coupling of the unpaired electrons in the two mental centers, broken symmetry calculations were performed. The configuration resulting from the computation at the PBE-D3/6-311++G(d,p)//PBE-D3/6-31G(d,p) level (PCM solvation included) had 238 kJ/mol higher electronic energy compared to the lowest-lying 10/2 state and the antiferromagnetic coupling was confirmed by the analysis of the Mulliken spin densities which had values of 2.6 and -2.9 a.u. on the Mn centers.

In the aqueous solution, the open axial coordination sites are likely to be occupied by H_2O molecules. Among the $H_2O[Mn_2(PhCOO)_4]H_2O$ complexes, the one with s=10/2 spin state, $\mathbf{1_{10/2}}$ complex (Fig. 1c), was energetically preferred, and the low-spin s=8/2 ($\mathbf{1_{8/2}}$) and 6/2 ($\mathbf{1_{6/2}}$) states had higher energies (43 and 54 kJ/mol correspondingly). Thereby, $\mathbf{1_{10/2}}$ formation from $[Mn_2(PhCOO)_4]$ complex in 10/2 spin state is exothermic by -84 kJ/mol. The formation of the antiferromagnetic state was unlikely in the case of $H_2O[Mn_2(PhCOO)_4]H_2O$ complex as well since the broken-symmetry computation at the PBE-D3/6-311++G(d,p)//PBE-D3/6-31G(d,p) level (PCM solvation included) shown that the singlet state had 332 kJ/mol higher energy compared to the 10/2 state. The Mulliken spin densities in Mn-centers in the singlet state were 4.5 and -4.5 a.u.

Water-bound cluster $\mathbf{1_{10/2}}$ (Scheme 1) was selected as the reference point and starting configuration for further modeling Mn-BTC interaction with the oxidizing species. It is worth noting

that the overlap between H_2O and $[Mn_2(PhCOO)_4]$ fragments in **$1_{10/2}$** is negligible (Fig. 1c), although the binding is highly exothermic (ΔE_{ads} = -84 kJ/mol). The coordination of H_2O molecules results in the formation of the four hydrogen bonds between OH-groups and the oxygen atoms of the carboxylate ligands. Thus, the highly exothermic effect of H_2O binding may be caused by the formation of strong hydrogen bonds and reduction of electrostatic repulsion between Mn^{2+}-cations due to the countering electrostatic field of H_2O dipoles.

Scheme 1 summarizes the chemical transformations that are considered here as potential pathways of oxidative degradation of Mn-BTC in the presence of O_2 or H_2O_2 species. The model oxidants are relevant to both biological and catalytic potential applications of Mn- and carboxylate-based metal-organic frameworks. Note, that depending on the spin-state, coordination complexes of different structures are formed; Scheme 1 explicitly indicates them with the appropriate labels. Fig. 2 graphically summarizes the relative energies of the oxidated complexes formation. These oxidative transformations are discussed in more detail in the subsequent sections.

3.2. O_2 binding

The binding of an O_2 molecule to the coordinately unsaturated Mn centers in Mn-BTC (**1→2**, Scheme 1) may result in two isomeric structures that are the end-on (η^1) and side-on (η^2) configurations. The end-on configuration is the result of the σ-type bonding of the O_2 molecule with Mn^{2+} cation while the side-on configuration is the complex having δ-type bond that corresponds to the binding of both oxygen atoms to the Mn^{2+} center. It should be noted that metal-ligand δ-symmetry bonding is somewhat unusual since it is usually observed in transition metal complexes having quadruple metal-metal-bond.[59]

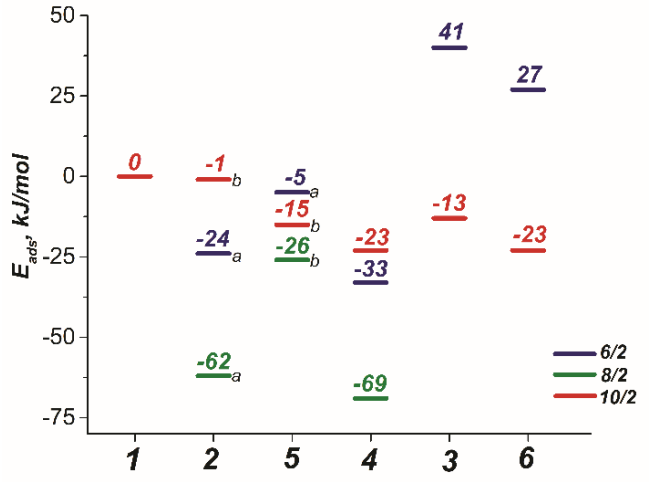

Figure 2. The concurrent adsorption energies (E_{ads}, see Section 2) of the O_2 and H_2O_2 oxidizing species to $H_2O[Mn_2(PhCOO)_4]H_2O$ complex.

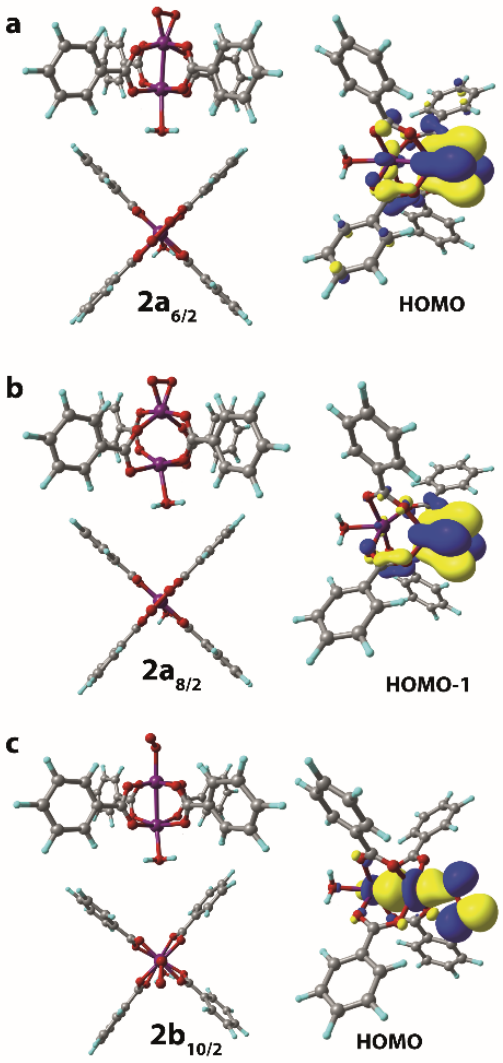

Figure 3. Geometries were optimized at the PBE-D3/6-31G(d,p) level of theory (front and side views are given). The key bonding MOs of the $O_2[Mn_2(PhCOO)_4]H_2O$ complexes in S = 6/2 (a), 8/2 (b), 10/2 (c) spin states are depicted with isosurface thresholds eq. 0.023.

The binding in both coordination modes results from the overlap between singly-occupied O_2 π^*-orbitals and 3d-orbitals of Mn that are singly-occupied as well, and the formation of the particular configuration leads to different spin states. Whereas the formation of η^1-complex preserves the spin state (with the corresponding structure is **$2b_{10/2}$**, see Scheme 1), the formation of δ-complexes with η^2-bound O_2 ligand leads to the electron pairing and the formation of **$2a_{6/2}$** and **$2a_{8/2}$** complexes in 6/2 and 8/2 spin states, respectively. The formation of the latter is strongly exothermic. The reaction energies computed for water exchange **1→2** are -24 and -62 kJ/mol for the formation of **$2a_{6/2}$** and **$2a_{8/2}$**, correspondingly (Fig. 2). The formation of σ-type bound **$2b_{10/2}$** complex in **1→2** process has a weak exothermic effect of -1 kJ/mol. The chemical irrelevance of the high-spin 12/2 state was ensured with the computed binding energy of 42 kJ/mol (see Fig S3a).

The complexation with O_2 distorts the initial square pyramidal geometry of the Mn centers in **$1_{10/2}$** to form a distorted octahedron in **$2a_{6/2}$** and trigonal bipyramid in **$2a_{8/2}$** of

O_2-coordinated Mn sites. The water-coordinated site in **$2a_{6/2}$** has octahedral geometry while H_2O-bonded Mn^{2+} center in **$2a_{8/2}$** has severely distorted trigonal-bipyramidal geometry with the cleaved Mn-Mn-bond. Mn-centers in **$2b_{10/2}$** form a highly distorted octahedrons (Fig. 3c).

The end-on-bound O_2-molecule in **$2b_{10/2}$** may formally be considered as a superoxide (O_2^-) ligand that implies the formal oxidation of Mn(+2) to Mn(+3). The formal oxidation state of oxygen-bound Mn-cations in **$2a_{6/2}$** and **$2a_{8/2}$** complexes then should be considered as Mn(+4) with the side-on bound peroxide (O_2^{2-}) ligands.

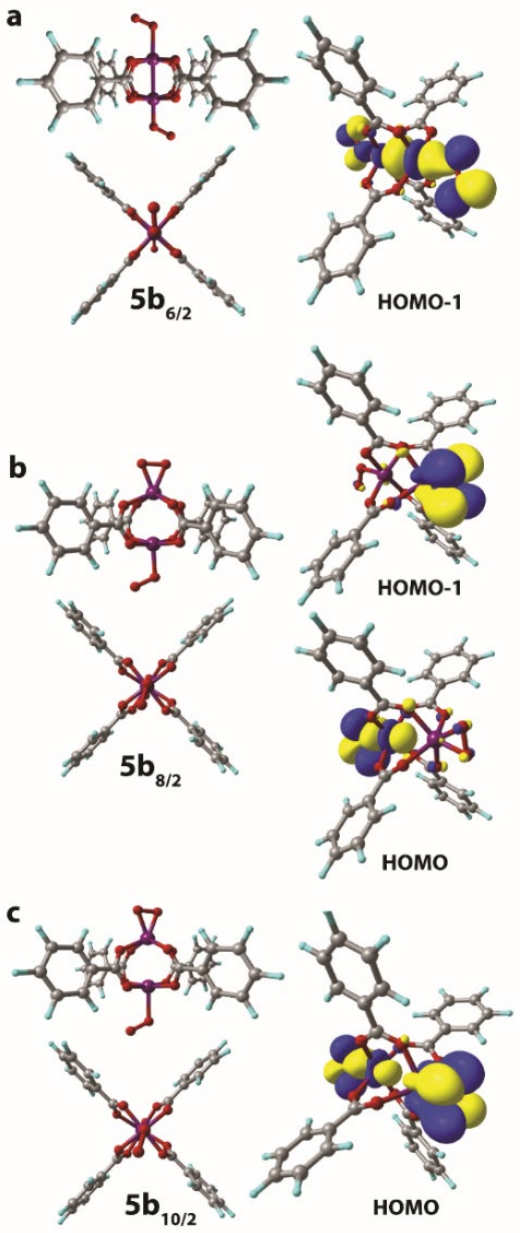

Figure 4. Geometries were optimized at the PBE-D3/6-31G(d,p) level of theory (front and side views are given). The key bonding MOs of the $O_2[Mn_2(PhCOO)_4]O_2$ complexes in s = 6/2 (a), 8/2 (b), 10/2 (c) spin states are depicted with isosurface thresholds eq. 0.023.

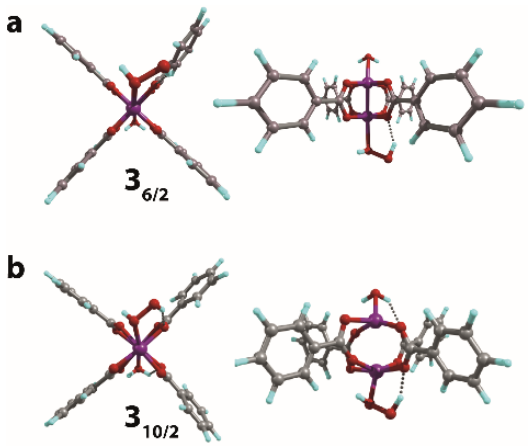

Figure 5. The geometries (front and side views) of the $H_2O[Mn_2(PhCOO)_4]H_2O_2$ complex in s = 6/2 (a) and 10/2 (b) spin states optimized at the PBE-D3/6-31G(d,p) level of theory.

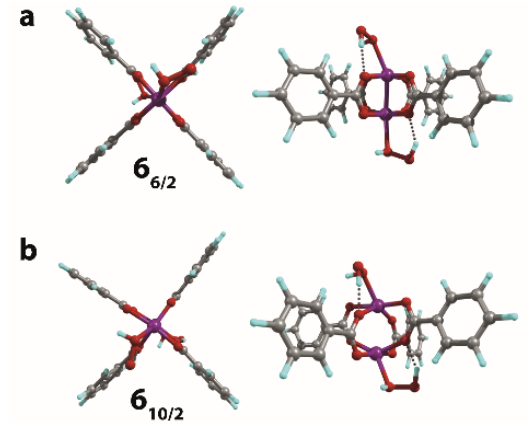

Figure 6. The geometries (front and side views) of the $H_2O_2[Mn_2(PhCOO)_4]H_2O_2$ complex in s = 6/2 (a) and 10/2 (b) spin states optimized at the PBE-D3/6-31G(d,p) level of theory.

The changes in the Mn oxidation states are in line with the Mulliken spin density changes in **1→2** reaction (Scheme 1). The O_2-binding in the case of $\mathbf{2_{10/2}}$ leads to the decrease of spin density on the interacting Mn (from 4.80 to 3.56) and the asymmetric decrease from (1, 1) to (0.70, 0.82) of the spin densities on O-atoms in O_2 molecule (see Table S2). Based on the analysis of the spatial distribution of Kohn-Sham orbitals, σ-symmetry bonding is evident when a single O-atom is bound to Mn. This implies the formation of a Mn-center in the formal (+3) oxidation state.

The δ-binding of the O_2-species proceeded via the electron density donation by Mn d-electrons to the π^*-orbitals of O_2 molecules resulting in the weakening of the O-O-bond. This is reflected in the significant increase of the O-O-bond in $\mathbf{2a_{8/2}}$ and $\mathbf{2a_{6/2}}$ structures (r(O-O) = 1.411 Å and 1.373 Å, respectively) when compared to that in dioxygen molecule (r(O-O) = 1.228 Å). The analysis of the electron density distribution in $\mathbf{2b_{6/2}}$ shown the decrease of spin density on oxygen atoms in O_2 molecule (from (1, 1) to (0.15, 0.15) a.u.) and the reduction of spin density values on the corresponding Mn-site (from 3.16 to 2.33). A similar trend was found in $\mathbf{2b_{8/2}}$ where spin densities on the Mn-site and the coordinated O_2 decreased from 3.28 to 2.94 and from (1, 1) to (0.11, 0.10), respectively (see Table S2). These changes indicate the formation of the Mn(+4) formal oxidation state in both cases.

The reaction of **2a** and **2b** complexes with a second O_2 molecule leads to the formation of two isomers (end-on-end-on and side-on-end-on) of the three possible ones (**2→5** step on the Scheme 1). The formation of side-on-side-on $O_2[Mn_2(PhCOO)_4]O_2$ isomer was not observed due to the significant steric strain of $[Mn_2(PhCOO)_4]$ core imposed by the side-on binding of O_2 species (see the discussion above and Fig. 3a-c).

The σ-type bonding of two oxygen molecules leads to an end-on-end-on configuration with the octahedral coordination of both Mn-cations. The formation of the corresponding $\mathbf{5a_{6/2}}$ complex proceeded with low exothermic effect of -5 kJ/mol (Fig. 4a). The side-on-end-on configuration corresponds to the simultaneous binding of O_2 species in δ- and σ-modes and the formation of $\mathbf{5a_{8/2}}$ and $\mathbf{5a_{10/2}}$ complexes is exothermic by -26 and -15 kJ/mol correspondingly (Fig. 4b-c). Here, both Mn centers adopt square pyramidal geometry.

The Mn centers having an η^2-bound O_2 ligand in $\mathbf{5_{8/2}}$ and $\mathbf{5_{10/2}}$ isomers were in Mn(+4) oxidation state as follows from the significant alternation of the spin densities upon their formation that is the spin density on the O atoms of the ligand changes from (1, 1) to (-0.27, -0.27) and (0.15, 0.15), respectively. At the same time, the spin density at the η^1-bound O_2 ligand in $\mathbf{5_{8/2}}$ and $\mathbf{5_{10/2}}$ changed from (1, 1) to (0.38, 0.46) and (0.78, 0.93), respectively, suggesting the oxidation of the metal center to the Mn(+3) state (see Table S2).

The $\mathbf{5_{14/2}}$ spin isomer corresponds to weak non-covalent bonding. Particularly, the lack of close Mn-O-contacts is evident in the optimized structures (see Fig. S3b) and the corresponding reaction energy is equal to 84 kJ/mol.

The Mn(+3) state is known to easily disproportionate leading to Mn(+2) and Mn(+4) formation in aqueous solutions.[60] Accordingly, our calculations show that the formation of η^1-bound O_2-complexes, that are the superoxide-bound (O_2^-) Mn(+3) cations in $L[Mn_2(PhCOO)_4]L$, is the least exothermic reaction ($\mathbf{5a_{6/2}}$ and $\mathbf{2_{10/2}}$ formation) among the alternative pathways. Therefore, we conclude that the oxidation of Mn-BTC MOF with O_2 forming Mn(+3) centers is less likely than the two-electron oxidation paths resulting in the oxidized structures with more stable Mn(+4) centers.

Compared to the exothermic step **1→2,** in which the first O_2 molecule binds, the binding of the second O_2 molecule is strongly endothermic. The formation of $\mathbf{5a_{6/2}}$ and $\mathbf{5a_{8/2}}$ increases the energies of the systems by 19 and 36 kJ/mol compared to $\mathbf{2a_{6/2}}$ and $\mathbf{2a_{8/2}}$, respectively. Only the σ-type bound complex $\mathbf{2a_{10/2}}$ formation is exothermic by -14 kJ/mol. The unfavorable binding of the second O_2 molecule in the cases of δ-complexes is supposedly a result of the distorted and, consequently, more sterically strained structure of the oxidized species. The results above on the facile oxidation and substantial structural distortions of the coordination sphere of Mn centers upon O_2 coordination imply that the degradation of Mn-BTC MOFs can be already induced at low O_2 concentrations creating thus an opportunity to develop O_2-selective response matrices as a basis for new smart drug delivery platforms.

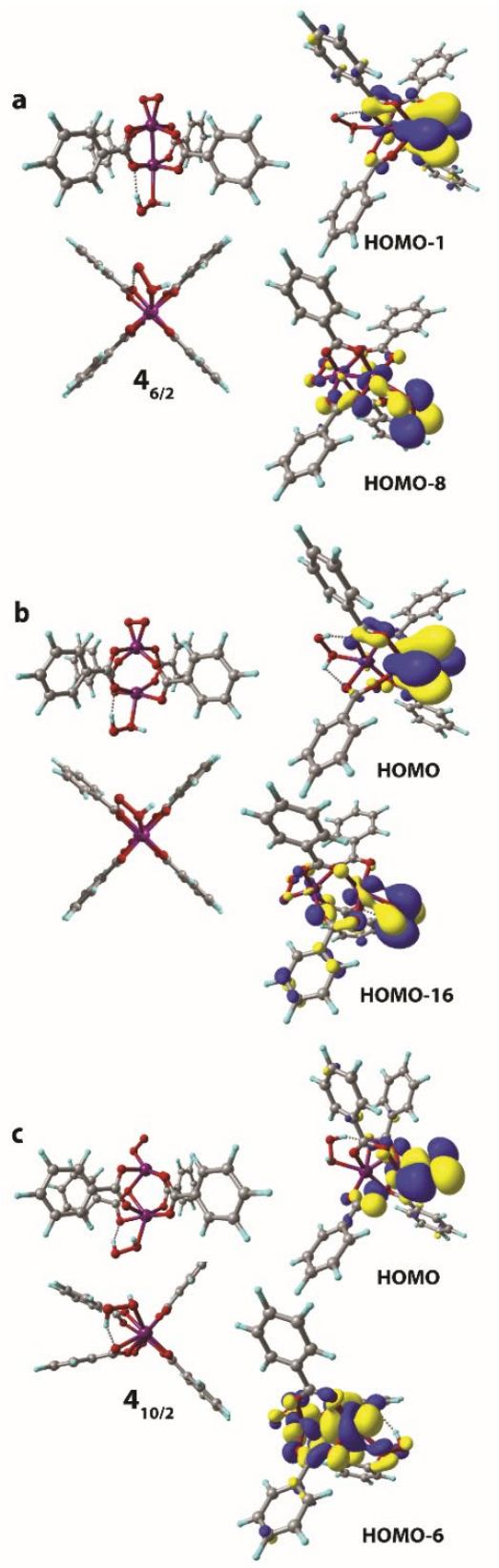

Figure 7. Geometries were optimized at the PBE-D3/6-31G(d,p) level of theory (front and side views are given). The key bonding MOs of the $H_2O_2[Mn_2(PhCOO)_4]O_2$ complex in s = 6/2 (a), 8/2 (b), 10/2 (c) spin states are depicted (isosurface tresholds are 0.023 (a), 0.023 for HOMO and 0.018 for HOMO-16 (b), 0.023 for HOMO and 0.018 for HOMO-6).

3.3. H_2O_2 binding

Next, we have investigated computationally the interaction of the Mn-BTC structure-forming unit $\mathbf{1_{10/2}}$ with H_2O_2 specie. The binding results in the formation of two spin isomers (namely, $\mathbf{3_{6/2}}$ and $\mathbf{3_{10/2}}$) via the **1→3** process. The isomers have the qualitatively close structures with H_2O_2 molecule bound in end-on configuration. The formation of the low-spin complex having the octahedral structure of Mn centers ($\mathbf{3_{6/2}}$, Fig. 5a) was highly endothermic with the reaction energy of 41 kJ/mol. The formation of the high-spin complex $\mathbf{3_{10/2}}$ was exothermic by -13 kJ/mol and the Mn center acquired a severely distorted trigonal-bipyramidal structure (Fig. 5b). The negligible change of the Mulliken spin density on the Mn-centers (from 3.16 to 3.14) and (from 4.80 to 4.77) for $\mathbf{3_{6/2}}$ and $\mathbf{3_{10/2}}$, respectively, illustrates a purely non-covalent nature of H_2O_2 binding that does not directly induce the oxidation of the Mn-centers (see Table S2).

The binding of the second H_2O_2 molecule via the **3→6** process proceeded with the retention of the coordination polyhedra and led to the formation of $\mathbf{6_{6/2}}$ and $\mathbf{6_{10/2}}$ (Fig. 6). These reactions had thermal effects of 27 and -23 kJ/mol, respectively.

The exchange of two water ligands with H_2O_2 leads to the coordination bond which is accompanied with a negligible decrease of the Mulliken spin density on the Mn centers in both $\mathbf{1_{10/2}}$→$\mathbf{6_{6/2}}$ and $\mathbf{1_{10/2}}$→$\mathbf{6_{10/2}}$ transformations (from 3.16 to 3.14 and from 4.80 to 4.77 respectively, see Table S2). These changes clearly show that the binding of H_2O_2 is not accompanied by the oxidation of the Mn-centers oxidation. The final complexes in the **1→3** and **3→6** steps are stabilized via the formation of the five-membered cycles with the hydrogen bonds between oxygen atoms of the carboxylate ligands and OH-groups of the bound H_2O_2 species (r(OH···O) = 1.7 – 2.0 Å). In the case of $\mathbf{6_{6/2}}$ and $\mathbf{6_{10/2}}$, two H_2O_2 molecules bound to both Mn-sites form two five-member cyclic structures contributing to their increased stability resulting in the thermodynamic favorability of the ligand exchange.

3.4. Combined O_2 and H_2O_2 binding

Finally, we have considered the possibility of the simultaneous binding of O_2 and H_2O_2 species via **1→4** process. The geometry optimization procedures resulted in a structure of only one structural type to be formed having η^2-bound O_2 and weakly (covalently) bound H_2O_2 molecules. The O_2-coordinated Mn sites in all **4** complexes adopted a trigonal-bipyramidal configuration (Fig. 7). High-spin $\mathbf{4_{10/2}}$ complex shown the highest degree of structural distortion upon the formation. Notably, the formation of all three possible complexes $\mathbf{4_{6/2}}$, $\mathbf{4_{8/2}}$, $\mathbf{4_{10/2}}$ was exothermic with the reaction energies of -33 kJ/mol, -69 kJ/mol and -23 kJ/mol respectively. The oxidation states of Mn centers in the formed $H_2O_2[Mn_2(PhCOO)_4]O_2$ complexes are (+2, +4), (+2, +4), and (+2, +4) correspondingly. The Kohn-Sham orbital and the Mulliken spin density analyses clearly illustrate the (+2, +4) formal oxidation states in both $\mathbf{4_{6/2}}$ and $\mathbf{4_{8/2}}$ spin isomers. Spin density values on O-atoms in O_2 ligand are notably reduced from (1, 1) to (0.15, 0.15) and (0.11, 0.11) in $\mathbf{4_{6/2}}$ and $\mathbf{4_{8/2}}$ respectively (see

Table S2). The spin density values on O_2-bound Mn-site decreased upon **$4_{6/2}$** (from 3.16 to 2.35) and **$4_{8/2}$** (from 3.28 to 2.91) formation. Less pronounced spin density changes were observed in the **$1_{10/2}$→$4_{10/2}$** process. Particularly, the change from 4.80 to 3.88 a.u. was observed on Mn-cation. In the case of O_2-ligand the observed change was from (1, 1) to (0.42 to 0.61) a.u. (Table S2). The key bonding orbital analysis (Fig. 7) corroborates the π-symmetry bonding and the formation of the Mn center in the (+4) formal oxidation state. The lower exothermicity of the **$4_{10/2}$** formation compared to the **$4_{6/2}$** and **$4_{8/2}$** isomers case is in line with lower orbital overlap (no δ-symmetry bond formed).

3.5. Reactivity

Degradation of the MOF material in aqueous solutions may potentially occur either via the direct hydrolysis of the metal-carboxylate moieties or via the oxidation of the metal-containing nodes. Whereas our calculations suggest that the latter mechanism should dominate the structural response Mn-BTC to the oxidative conditions in the presence of molecular O_2, the mechanism of MOF degradation in the presence of H_2O_2 as the oxidant requires the combination of the metal oxidation with hydrolytic process. Indeed, no significant deformations of the [Mn_2(PhCOO)$_4$] structural unit was observed upon H_2O_2 binding. The coordinatively unsaturated metal centers in the [Mn_2(PhCOO)$_4$] cluster tend to bind strongly the open-shell O_2 species due to the radical nature of the former. The degradation of Mn-BTC via the oxidation by H_2O_2 closed-shell species may have a more complex mechanism. The adsorption complexes **6** discussed above thus become the starting point for the computational assessment of the feasibility of such a complex oxidation-assisted hydrolysis mechanism.

The oxidation-assisted hydrolysis thus starts with the substitution of the water molecules in the solvated **$1_{10/2}$** structure discussed in detail previously and the formed **$6_{6/2}$** and **$6_{10/2}$** intermediates undergo the further oxidation (Fig. 6). The transition state on the potential energy surface with 10/2 spin state is denoted as **$TS_{10/2}$** and corresponds to the barrier of 21 kJ/mol. The computed imaginary frequency of **$TS_{10/2}$** structure has the value of i365 cm^{-1} corresponding to the O-O-bond stretching in the H_2O_2 moiety and the neighbouring Mn site has the trigonal-bipyramidal coordination polyhedron. After passing **$TS_{10/2}$**, the relative order of the potential energy surfaces with S = 10/2 and 6/2 changes and the system may undergo a spin crossing.

For the high-spin complex **$7_{10/2}$**, the O-O-bond cleavage in the peroxide moiety leads to Mn(+4) center formation which has octahedral geometry and bears two terminal OH ligands. The oxidation is accompanied with the reduction of the Mulliken spin density value in the Mn-center (4.78 to 3.90 a.u., see Table S3). The reaction energy for the latter process is -87 kJ/mol. The subsequent hydrolysis leads to H_2O binding to the Mn(+4) site through the formation of the hydrogen bonds between H-atoms of H_2O molecule and O-sites of the hydroxyl- and benzoate-ligands. The corresponding intermediate is denoted as **$8_{10/2}$** (Fig. 8). The non-valent H_2O molecule coordination does not alter the octahedral geometry of the Mn(+4) centers.

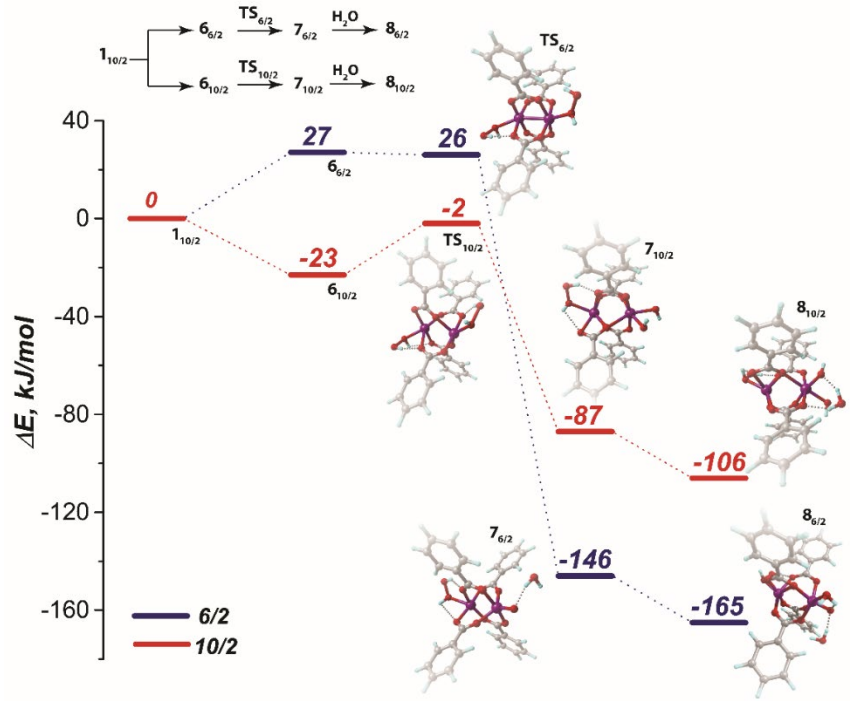

Figure 8. Reaction energy profiles for the oxidation-induced hydrolysis of **$6_{6/2}$** and **$6_{10/2}$**. The optimized structutures of the initial (**$6_{6/2}$**, **$6_{10/2}$**), transition (**$TS_{6/2}$**, **$TS_{10/2}$**), final oxidized (**$7_{6/2}$**, **$7_{10/2}$**) and hydrolyzed states (**$8_{6/2}$**, **$8_{10/2}$**) are presented next to the corresponding energy levels. All geometries were optimized at the PBE-D3/6-31G(d,p) level of theory.

The Mn-BTC degradation via 6/2 pathway was thermodynamically preferred according to the modeling results. The $\mathbf{7_{6/2}}$ intermediate had the energy that is lower by -146 kJ/mol relative to $\mathbf{1_{10/2}}$ level and by -59 kJ/mol relative to the $\mathbf{7_{10/2}}$ counterpart. We expect the $\mathbf{6_{6/2}}$ to $\mathbf{7_{6/2}}$ transition to be barrierless. Particularly, the "barrier" of -1 kJ/mol, that was computed at the PBE-D3/6-311++G(d,p)//PBE-D3/6-31G(d,p) level with PCM solvation model, could be the inaccuracy caused by the solvation model which was applied in post-optimization single-point energy refinement. The imaginary mode in $\mathbf{TS_{6/2}}$ structure corresponded to O-O-bond stretching and had the frequency of *i*261 cm^{-1} as computed at the PBE-D3/6-31G(d,p) level of theory. The oxidized Mn(+4) center in the $\mathbf{7_{6/2}}$ intermediate had the trigonal-bipyramidal structure bearing the oxo-ligand. The spin density value decreased from 3.14 to 2.33 a.u. in $\mathbf{6_{6/2}}\rightarrow\mathbf{7_{6/2}}$ (see Tables S3). Then oxidized $\mathbf{7_{6/2}}$ specie underwent a strongly exothermic (ΔE = –165 kJ/mol) hydrolysis step. The Mn center adopted the octahedral coordination in the $\mathbf{8_{6/2}}$ intermediate formed upon the hydrolysis.

The structural flexibility of the unconstrained cluster model provides sufficient space for the relaxation upon the interaction with the oxidative species needed to ensure the overall stability of the extended periodic structure composed of such units. Here we infer that the potential degradation paths are initiated when the ROS binding induces severe structural deformations that substantially alter the coordination polyhedra of the Mn sites. Although the introduction of the hard geometric constraints decreased the exothermicity of the adsorption complexes formation (Fig. S1 and Table S1), the effects were minor and did not affect the main conclusions made on the basis of the fully relaxed models consideration that have been discussed above. In some cases, we, however, observed the enhancement of the reactivity of the Mn sites due to the excessive strain provided by the constrained benzoate ligands, which resulted in some cases in the decoordination events and structural alternation of the otherwise stable geometries (Fig. S2). These effects appear to be highly model-dependent and are not expected to be representative to the sufficiently flexible MOF structures that is captured by the relaxed cluster models.

Conclusions

Density functional theory calculations have been performed to investigate the interactions of common oxidants (O_2 and H_2O_2) with a cluster model representing the key structural fragment of Mn-BTC MOF. The modeling was performed to assess potential material degradation paths under the oxidizing conditions commonly encountered in pathogenic tissues of living organisms. Such an environment-induced degradation of the nanoporous material was discussed in the context of the development of new approaches for the targeted drug delivery.

The calculations indicated a sufficient stability of the Mn-carboxylate structure-forming units towards the direct hydrolysis while the interaction with the O_2 and H_2O_2 species led to a facile oxidation of the Mn(+2) to the more thermodynamically stable Mn(+4) state. The oxidation was proceeded with a substantial deformation of the coordination sphere of the transition metal centers and, accordingly, facilitation of the subsequent hydrolysis of the coordination bonds.

DFT calculations shown a facile exchange of non-covalently bound H_2O ligands at the Mn(+2) centers in the Mn-BTC with molecular O_2 resulting in a covalent σ-, π-, or δ-binding. The latter path was more favorable and it resulted in the oxidation of the Mn center to the formal (+4) state and the formation of a peroxide adduct. The formation of the Mn(+3) state was the result of the O_2 ligand complexation in the σ-binding mode and was likely the intermediate state in the formation of the more stable Mn(+4) counterpart.

On the contrary, hydrogen peroxide molecules bind weakly to the Mn sites. The respective ligand exchange reaction with the starting aqua-complex was an exothermic process for the high-lying spin state. The H_2O_2-induced degradation of Mn-BTC in aqueous media involved the cleavage of the O-O bond in the coordinated H_2O_2 molecules resulting in the oxidation of the Mn(+2) center to the (+4) state that strongly facilitated the subsequent hydrolysis. Importantly, we note the importance of spin-transitions for all reaction paths considered in this study. This has to be properly accounted in further studies on the stability of Mn-based MOF materials. Our current results clearly show the limited potential of Mn-carboxylate building blocks for oxidation catalysis or gas-sorption applications where the interactions with potential ROS species will inevitably result in the structural distortion of the framework and the long-term degradation of the functional materials. Nevertheless, the favorable reaction paths identified here may be utilized for engineering a new mechanism of structural response of the Mn-containing nanocontainers to pathology-induced alternations of biological environments.

Conflicts of interest

There are no conflicts to declare

Acknowledgements

This work was supported by the Ministry of Education and Science of Russian Federation (Project 11.1706.2017/4.6). E.A.P. acknowledges a partial support from the European Research Council (ERC) under the European Union's Horizon 2020 research and innovation programme (grant agreement No. 725686). A.V.V. acknowledges the support from the Government of the Russian Federation (Grant 08-08). The Netherlands Organization for Scientific Research (NWO) is acknowledged for providing access to the supercomputer facilities.

References

1 P. W. Siu, J. P. Siegfried, M. H. Weston, P. E. Fuller, W. Morris, C. R. Murdock, W. J. Hoover, R. K. Richardson, S. Rodriguez and O. K. Farha, Boron Trifluoride Gas Adsorption in Metal-Organic Frameworks, *Inorg. Chem.*,

2016, **55**, 12110–12113.
2 T. Simon-Yarza, S. Rojas, P. Horcajada and C. Serre, *The Situation of Metal-Organic Frameworks in Biomedicine*, Elsevier, 2017.
3 J. S. Choi, W. J. Son, J. Kim and W. S. Ahn, *Microporous Mesoporous Mater.*, 2008, **116**, 727–731.
4 N. Wei, Y. Zhang, L. Liu, Z. B. Han and D. Q. Yuan, Pentanuclear Yb(III) cluster-based metal-organic frameworks as heterogeneous catalysts for CO_2 conversion, *Appl. Catal. B Environ.*, 2017, **219**, 603–610.
5 T. Rodenas, I. Luz, G. Prieto, B. Seoane, H. Miro, A. Corma, F. Kapteijn, F. X. Llabrés I Xamena and J. Gascon, Metal-organic framework nanosheets in polymer composite materials for gas separation, *Nat. Mater.*, 2015, **14**, 48–55.
6 Z.-G. Gu, S. Grosjean, S. Bräse, C. Wöll and L. Heinke, Enantioselective adsorption in homochiral metal–organic frameworks: the pore size influence, *Chem. Commun.*, 2015, **51**, 8998–9001.
7 L. R. Mingabudinova, V. V. Vinogradov, V. A. Milichko, E. Hey-Hawkins and A. V. Vinogradov, Metal–organic frameworks as competitive materials for non-linear optics, *Chem. Soc. Rev.*, 2016, **45**, 5408–5431.
8 Y.-B. Huang, J. Liang, X.-S. Wang and R. Cao, Multifunctional metal–organic framework catalysts: synergistic catalysis and tandem reactions, *Chem. Soc. Rev.*, 2017, **46**, 126–157.
9 L. Zhu, X. Q. Liu, H. L. Jiang and L. B. Sun, *Chem. Rev.*, 2017, 117, 8129–8176.
10 D. Damasceno Borges, G. Maurin and D. S. Galvão, Design of Porous Metal-Organic Frameworks for Adsorption Driven Thermal Batteries, *MRS Adv.*, 2017, **2**, 519–524.
11 J. J. Low, A. I. Benin, P. Jakubczak, J. F. Abrahamian, S. A. Faheem and R. R. Willis, Virtual high throughput screening confirmed experimentally: Porous coordination polymer hydration, *J. Am. Chem. Soc.*, 2009, **131**, 15834–15842.
12 I. J. Kang, N. A. Khan, E. Haque and S. H. Jhung, Chemical and thermal stability of isotypic metal-organic frameworks: Effect of metal ions, *Chem. Eur. J.*, 2011, **17**, 6437–6442.
13 C. Y. Sun, C. Qin, C. G. Wang, Z. M. Su, S. Wang, X. L. Wang, G. S. Yang, K. Z. Shao, Y. Q. Lan and E. B. Wang, Chiral nanoporous metal-organic frameworks with high porosity as materials for drug delivery, *Adv. Mater.*, 2011, **23**, 5629–5632.
14 A. C. McKinlay, R. E. Morris, P. Horcajada, G. Férey, R. Gref, P. Couvreur and C. Serre, *Angew. Chem. Int. Ed.*, 2010, 49, 6260–6266.
15 M. Giménez-Marqués, T. Hidalgo, C. Serre and P. Horcajada, *Coord. Chem. Rev.*, 2015.
16 E. Bellido, M. Guillevic, T. Hidalgo, M. J. Santander-Ortega, C. Serre and P. Horcajada, Understanding the colloidal stability of the mesoporous MIL-100(Fe) nanoparticles in physiological media, *Langmuir*, 2014, **30**, 5911–5920.
17 K. M. L. Taylor-Pashow, J. Della Rocca, Z. Xie, S. Tran and W. Lin, Postsynthetic modifications of iron-carboxylate nanoscale metal-organic frameworks for imaging and drug delivery, *J. Am. Chem. Soc.*, 2009, **131**, 14261–14263.
18 J. Della Rocca, D. Liu and W. Lin, Nanoscale metal-organic frameworks for biomedical imaging and drug delivery, *Acc. Chem. Res.*, 2011, **44**, 957–968.
19 R. Ananthoji, J. F. Eubank, F. Nouar, H. Mouttaki, M. Eddaoudi and J. P. Harmon, Symbiosis of zeolite-like metal–organic frameworks (rho-ZMOF) and hydrogels: Composites for controlled drug release, *J. Mater. Chem.*, 2011, **21**, 9587.
20 P. Horcajada, T. Chalati, C. Serre, B. Gillet, C. Sebrie, T. Baati, J. F. Eubank, D. Heurtaux, P. Clayette, C. Kreuz, J. S. Chang, Y. K. Hwang, V. Marsaud, P. N. Bories, L. Cynober, S. Gil, G. Férey, P. Couvreur and R. Gref, Porous metal-organic-framework nanoscale carriers as a potential platform for drug deliveryand imaging, *Nat. Mater.*, 2010, **9**, 172–178.
21 C.-Y. Sun, C. Qin, X.-L. Wang and Z.-M. Su, Metal-organic frameworks as potential drug delivery systems, *Expert Opin. Drug Deliv.*, 2013, **10**, 89–101.
22 S. Fu, C. Zhu, J. Song, D. Du and Y. Lin, *Adv. Energy Mater.*, 2017, 7.
23 P. Canepa, K. Tan, Y. Du, H. Lu, Y. J. Chabal and T. Thonhauser, Structural, elastic, thermal, and electronic responses of small-molecule-loaded metal–organic framework materials, *J. Mater. Chem. A*, 2015, **3**, 986–995.
24 J. a Kellum, M. Song and J. Li, Science review: extracellular acidosis and the immune response: clinical and physiologic implications., *Crit. Care*, 2004, **8**, 331–336.
25 P. J. Barnes, *Free Radic. Biol. Med.*, 1990, 9, 235–243.
26 M. Mittal, M. R. Siddiqui, K. Tran, S. P. Reddy and A. B. Malik, Reactive Oxygen Species in Inflammation and Tissue Injury, *Antioxid. Redox Signal.*, 2014, **20**, 1126–1167.
27 P. Horcajada, C. Serre, G. Maurin, N. A. Ramsahye, F. Balas, M. Vallet-Regí, M. Sebban, F. Taulelle and G. Férey, Flexible porous metal-organic frameworks for a controlled drug delivery, *J. Am. Chem. Soc.*, 2008, **130**, 6774–6780.
28 K. S. Egorova and V. P. Ananikov, Toxicity of Metal Compounds: Knowledge and Myths, *Organometallics*, 2017, **36**, 4071–4090.
29 G. C. Dismukes, Manganese Enzymes with Binuclear Active Sites, *Chem. Rev.*, 1996, **96**, 2909–2926.
30 N. A. Law, M. T. Caudle and V. L. Pecoraro, Manganese Redox Enzymes and Model Systems: Properties, Structures, and Reactivity, *Adv. Inorg. Chem.*, 1998, **46**, 305–440.
31 G. D. Lawrence and D. T. Sawyer, The chemistry of biological manganese, *Coord. Chem. Rev.*, 1978, **27**, 173–193.
32 T. Ladrak, S. Smulders, O. Roubeau, S. J. Teat, P. Gamez and J. Reedijk, Manganese-based metal-organic frameworks as heterogeneous catalysts for the cyanosilylation of acetaldehyde, *Eur. J. Inorg. Chem.*, 2010, 3804–3812.
33 Q. Sun, M. Liu, K. Li, Y. Han, Y. Zuo, F. Chai, C. Song, G. Zhang and X. Guo, Synthesis of Fe/M (M = Mn, Co, Ni) bimetallic metal organic frameworks and their catalytic activity for phenol degradation under mild conditions, *Inorg. Chem. Front.*, 2017, **4**, 144–153.
34 C. Pereira, M. Simoes, J. Tome and F. Almeida Paz, Porphyrin-Based Metal-Organic Frameworks as Heterogeneous Catalysts in Oxidation Reactions,

Molecules, 2016, **21**, 1348.

35 Y. Ming, J. Purewal, J. Yang, C. Xu, R. Soltis, J. Warner, M. Veenstra, M. Gaab, U. Müller and D. J. Siegel, Kinetic stability of MOF-5 in humid environments: Impact of powder densification, humidity level, and exposure time, *Langmuir*, 2015, **31**, 4988–4995.

36 P. Guo, D. Dutta, A. G. Wong-Foy, D. W. Gidley and A. J. Matzger, *J. Am. Chem. Soc.*, 2015, 137, 2651–2657.

37 A. Dhakshinamoorthy, M. Alvaro and H. Garcia, Metal–organic frameworks as heterogeneous catalysts for oxidation reactions, *Catal. Sci. Technol.*, 2011, **1**, 856.

38 S. Zuluaga, E. M. A. Fuentes-Fernandez, K. Tan, F. Xu, J. Li, Y. J. Chabal and T. Thonhauser, Understanding and controlling water stability of MOF-74, *J. Mater. Chem. A*, 2016, **4**, 5176–5183.

39 D. Wu, W. Yan, H. Xu, E. Zhang and Q. Li, Defect engineering of Mn-based MOFs with rod-shaped building units by organic linker fragmentation, *Inorg. Chim. Acta*, 2017, **460**, 93–98.

40 Y. Kuwahara, Y. Yoshimura and H. Yamashita, Liquid-phase oxidation of alkylaromatics to aromatic ketones with molecular oxygen over a Mn-based metal–organic framework, *Dalton Trans.*, 2017, **46**, 8415–8421.

41 R. E. Hansen and S. Das, Biomimetic di-manganese catalyst cage-isolated in a MOF: robust catalyst for water oxidation with Ce^{iv}, a non-O-donating oxidant, *Energy Environ. Sci.*, 2014, **7**, 317–322.

42 D. H. Lee, S. Kim, M. Y. Hyun, J.-Y. Hong, S. Huh, C. Kim and S. J. Lee, Controlled growth of narrowly dispersed nanosize hexagonal MOF rods from Mn(III)–porphyrin and $In(NO_3)_3$ and their application in olefin oxidation, *Chem. Commun.*, 2012, **48**, 5512.

43 S. Bhattacharjee, D.-A. Yang and W.-S. Ahn, A new heterogeneous catalyst for epoxidation of alkenes via one-step post-functionalization of IRMOF-3 with a manganese(ii) acetylacetonate complex, *Chem. Commun.*, 2011, **47**, 3637.

44 J. Ye and C. Liu, $Cu_3(BTC)_2$: CO oxidation over MOF based catalysts, *Chem. Commun.*, 2011, **47**, 2167.

45 K. Brown, S. Zolezzi, P. Aguirre, D. Venegas-Yazigi, V. Paredes-García, R. Baggio, M. A. Novak and E. Spodine, $[Cu(H_2btec)(bipy)]_\infty$: a novel metal organic framework (MOF) as heterogeneous catalyst for the oxidation of olefins, *Dalton Trans.*, 2009, 1422.

46 K. K. Tanabe and S. M. Cohen, Engineering a metal-organic framework catalyst by using postsynthetic modification, *Angew. Chem. Int. Ed.*, 2009, **48**, 7424–7427.

47 M. Zhang, X. Huang and Y. Chen, DFT insights into the adsorption of NH_3-SCR related small gases in Mn-MOF-74, *Phys. Chem. Chem. Phys.*, 2016, **18**, 28854–28863.

48 P. Maitarad, S. Namuangruk, D. Zhang, L. Shi, H. Li, L. Huang, B. Boekfa and M. Ehara, Metal-porphyrin: A potential catalyst for direct decomposition of N_2O by theoretical reaction mechanism investigation, *Environ. Sci. Technol.*, 2014, **48**, 7101–7110.

49 P. Maitarad, J. Meeprasert, L. Shi, J. Limtrakul, D. Zhang and S. Namuangruk, Mechanistic insight into the selective catalytic reduction of NO by NH_3 over low-valent titanium-porphyrin: A DFT study, *Catal. Sci. Technol.*, 2016, **6**, 3878–3885.

50 M. J. et al Frisch, *Gaussian 09, Revis. D.01*, 2009.

51 V. V Vinogradov, A. S. Drozdov, L. mingabudinova, E. M. Shabanova, N. Kolchina, E. I. Anastasova, A. A. Markova, A. Shtil, V. Milichko, galina L. starova, R. Precker, A. Vinogradov, E. Hey-Hawkins and E. Pidko, Composites Based on Heparin and MIL-101(Fe): The Drug Releasing Depot for Anticoagulant Therapy and Advanced Medical Nanofabrication, *J. Mater. Chem. B*, 2018.

52 J. P. Perdew, K. Burke and M. Ernzerhof, Generalized Gradient Approximation Made Simple, *Phys. Rev. Lett.*, 1996, **77**, 3865–3868.

53 S. Grimme, J. Antony, S. Ehrlich and H. Krieg, A consistent and accurate ab initio parametrization of density functional dispersion correction (DFT-D) for the 94 elements H-Pu, *J. Chem. Phys.*, , DOI:10.1063/1.3382344.

54 S. Grimme, Semiempirical GGA-type density functional constructed with a long-range dispersion correction, *J. Comput. Chem.*, 2006, **27**, 1787–1799.

55 S. Miertuš, E. Scrocco and J. Tomasi, Electrostatic interaction of a solute with a continuum. A direct utilizaion of ab initio molecular potentials for the prevision of solvent effects, *Chem. Phys.*, 1981, **55**, 117–129.

56 E. Stavitski, E. A. Pidko, S. Couck, T. Remy, E. J. M. Hensen, B. M. Weckhuysen, J. Denayer, J. Gascon and F. Kapteijn, Complexity behind CO_2 capture on NH_2-MIL-53(Al), *Langmuir*, 2011, **27**, 3970–3976.

57 J. Van Den Bergh, C. Gücüyener, E. A. Pidko, E. J. M. Hensen, J. Gascon and F. Kapteijn, Understanding the anomalous alkane selectivity of ZIF-7 in the separation of light alkane/alkene mixtures, *Chem. A Eur. J.*, 2011, **17**, 8832–8840.

58 Chemcraft, http://www.chemcraftprog.com, (accessed 5 January 2018).

59 L. R. Falvello, B. M. Foxman and C. A. Murillo, Fitting the Pieces of the Puzzle: The δ Bond, *Inorg. Chem.*, 2014, **53**, 9441–9456.

60 C. E. Housecroft and A. G. Sharpe, *Inorganic Chemistry*, 2012.

Table of Contents